Journal of Magnetic Resonance **140,** 17–31 (1999)
Article ID jmre.1999.1828, available online at http://www.idealibrary.com on IDEAL®

Error-Tolerant RF Litz Coils for NMR/MRI

F. David Doty, George Entzminger Jr., and Cory D. Hauck

Doty Scientific, Inc., Columbia, South Carolina 29229

Received January 20, 1999; revised May 26, 1999

A new class of NMR RF volume coils is being developed that permits improved tuning range, B_1 homogeneity, tuning stability, and sensitivity compared to birdcages over a wide range of practical conditions, especially for microscopy and wraparound flexible applications. They are denoted litz coils, as their flux transparency and current distribution is obtained from woven foil patterns with insulated crossovers. Contrary to the design criteria of phased arrays, the parallel routes in litz coils use high coupling coefficients to achieve optimal current distribution, which is highly independent of tuning, balancing, and matching adjustments and is compatible with multiple capacitive segmentation. Magnetic filling factors, loaded Q, and inhomogeneity measurements and calculations are presented for a variety of litz coils with frequency-diameter products from 7 to 20 MHz-m and are compared to similar birdcages.

Key Words: **litz coil; birdcage; double-resonance; multinuclear.**

INTRODUCTION

The birdcage RF volume coil (*1, 2*) and variations thereof (*3*) can achieve high homogeneity and high sensitivity over a wide range of conditions. However, sample-dependent loading and tuning shifts often seriously impair performance, especially with larger coils at higher frequencies, even though fixed tuning asymmetries are correctable (*4*). For example, we have recently shown that asymmetric sample loading may easily produce rung current errors exceeding 20% (even after a first-order correction) in 100-mm-diameter birdcages at 200 MHz and that accurate correction of sample-dependent effects at frequency-diameter (*fd*) products of only 20 MHz-m typically requires a complex series of adjustments of 6 to 14 variable capacitors (*5*). This procedure is seldom justified in clinical settings, and the resulting image degradation is accepted. However, high-field research applications are often more demanding. Moreover, since a recent calculation concluded that a typical 1.5-T whole body magnetic resonance (MR) coil achieved only 36% of ultimate achievable SNR at the center of the sample (*6*), there is reason to believe that substantial progress in coil design is still possible.

Our motivation for exploring novel current topologies for improved performance (tuneability, homogeneity, and S/N) arose primarily from our experience in servicing researchers of mice and rat models in high-field vertical bore magnets (7 to 12 T) in labs where it was often important to quickly obtain high B_1 homogeneity with a variety of asymmetric loads, even with double-resonance ^{1}H–^{19}F MR spectroscopy applications. Our experience showed that the classic NMR S/N dependence at a given frequency, $(\eta_F Q_L)^{1/2}$ (where η_F is the magnetic filling factor and Q_L is the loaded Q) is a more reliable indicator of sensitivity than the ratio of unloaded to loaded Q, Q_0/Q_L. Hence, our approach was to first develop software that permitted rapid and accurate calculations of η_F, mean B_1 inhomogeneity σ, and current distributions across parallel inductors for arbitrary coil assemblies using an augmented Biot-Savart method (*5, 7, 8*). The software also permitted estimates of Q_L.

We calculate the average variation σ in the absolute value of the transverse B_1 component expressed as a percentage of mean B_1 throughout a specified sample volume according to a common definition (*9*). Filling factor is defined as the magnetic energy in the *rotating* component B_1 of the magnetic field throughout the sample divided by the total magnetic energy T throughout all space:

$$\eta_F = \frac{\int_s B_1^2 dV}{2\mu_0 T}. \qquad [1]$$

For linear polarization, filling factor is then half of the energy of the transverse component in the sample divided by the total energy. A simple method for directly measuring η_F has recently been described (*5, 10*) that makes it easy to check the numerical calculations.

The initial conceptual design approach was to explore coils related to the Alderman–Grant resonator (*11*), where the current distribution (hence, σ) was essentially independent of capacitor matching and phase shifts, as this appeared to be the most practical route to tuning simplifications with variable loads. We were quite surprised to find the calculated η_F for birdcages often below 6%, while the filling factor of the Alderman–Grant resonator with the Kost 90° window optimization (*12*) was often comparable (even after dividing by 2 to correct for the difference between circular and linear polarization), and Q_L for small *fd* was generally higher. Bench measurements confirmed the numerical calculations, and analytical

1090-7807/99 $30.00

TABLE 1
Error-Tolerant 100-mm Linear Resonators

Experiment No.	1	2	3	4	5	6	7	8	9
Coil type	KAG	SHT	CFL2	CFL2	CFL2	CFL4	CFL4	CFL6	CFL6
f_0, MHz	124	74	68.5	70	104	134	200	200	200
ROI, dia. × lgh, mm^2	78 × 78	78 × 80	80 × 80	80 × 70	80 × 70	80 × 70	80 × 70	80 × 60	80 × 70
Overall lgh, mm	170	162	165	136	136	136	136	143	136
Window lgh, mm	82	90	65	55	55	55	55	47	55
Shield dia, mm	140	200	140	140	140	140	140	200	140
C_T, pF, meas	33	39	47	47	16	22	8.2	11	15
Q_0, meas	434	173	427	477	474	520	453	424	495
Q_{LS}, sphere, meas	243	140	291	269	242	222	186	211	179
Q_L, cyl, meas	73	55	98	114	76	58	43	44	64
η_F, %, calc	5.9	7.5	6.1	5.9	5.9	5.9	5.9	9	5.9
η_F, %, meas	3.2	6.9	5.3	4.7	4.6	4.9	4.4	7	4.8
$f_{\Delta T}$, %, meas	0.8	1.8	1.3	2.4	2.7	2.1	4	5	2.7
σ, %, calc	9.5	8.2	7.7	7.8	7.8	7.8	7.8	7.8	7.8
$(\eta_F Q_L)^{1/2}$, meas	15.3	19.5	22.8	23.1	18.7	16.9	13.7	17.5	17.5
τ_{90} (μs) @ 1 kW	58	36	30	28	42	53	80	58	63

Note. Data are for linear polarization. See text for abbreviations and descriptions.

calculations on several simple coils (*5*) further verified the accuracy of the software in the long wavelength approximation.

The next step was to realize that the homogeneity limitation of the slotted resonator and related coils comes from the tendency of the current to concentrate near the edge of the flux-windows. However, this behavior can be controlled from the use of parallel foil conductors with insulated crossovers that force the current to redistribute in a more optimal manner. The use of woven, insulated foil conductors is reminiscent of the use of braided (or woven) insulated wire commonly known as "litz" wire (from the old German for braided) in some high-Q RF coils—although the purpose is different. Hence, we denote this new family of NMR coils as litz coils.

The litz foil coils have thus far demonstrated substantial improvements in tuning simplicity and in B_1 homogeneity at frequencies from 10 to 600 MHz and coil sizes from 6 to 300 mm, and they are expected to maintain these advantages in larger coils. Where comparable data are currently available, we obtain higher sensitivity and homogeneity with a *linear* litz coil than with a *quadrature* birdcage under otherwise identical conditions. Before looking at the complex foil patterns of the litz coil, however, it is useful to take a closer look at the Alderman–Grant resonator and related coils as a point of departure.

OPTIMIZED SLOTTED RESONATORS: THE KOST-OPTIMIZED ALDERMAN–GRANT (KAG) AND SPLIT-HALF-TURN (SHT) COILS

Table 1 shows measured and calculated data (Q_0, Q_L, η_F, and σ) for a number of experiments with 100-mm linear resonators fabricated from 0.06-mm copper foil with overall lengths, window lengths, and shield diameters as indicated. The filling factors and σ shown are for the cylindrical homogeneous region of interest (ROI). Loaded Q measurements, Q_{LS} and Q_L, are shown respectively for both a 70-mm sphere and a large, asymmetrically placed, cylindrical saline sample (35 mM) that extends from one end of the ROI to at least one radius beyond the other end of the ROI. The relative tuning shift $f_{\Delta T}$ produced by the large saline sample is given as a percentage of f_0. The data may be readily compared to that for similar, quadrature birdcages (*5*), where the same methods were used for all measurements and calculations.

The B_1 homogeneity σ of the Kost-optimized Alderman–Grant resonator with a large sample is found to be 9.5%, which is slightly better than that of the eight-rung balanced-high-pass (BHP) birdcage when typical sample-dependent effects on coupling and tuning asymmetries are included, where σ (for the same sample and shield diameters) was shown to be 10.3% (*5*). Also, the $\eta_F Q_L$ product of the KAG coil is generally higher for fd below 8 MHz-m. Since this coil is much easier to tune, it is not surprising that it (or a close relative, such as is described next) continues to be the resonator of choice in probably 95% of high-field spectroscopy applications for fd in the range of 3 to 8 MHz-m. (The rather large discrepancy between the measured and calculated values of η_F shown for the KAG coil in experiment 1 decreased at lower frequencies.) The primary drawback of the KAG coil is that it lacks transverse transparency so it cannot be used effectively with an orthogonal coil without a minor modification. Of course, its sensitivity may be up to 30% less than that of the circular-polarization birdcage at much larger fd.

Figure 1 illustrates the foil pattern for a simple improvement on the KAG coil which we designate as the SHT saddle coil. It

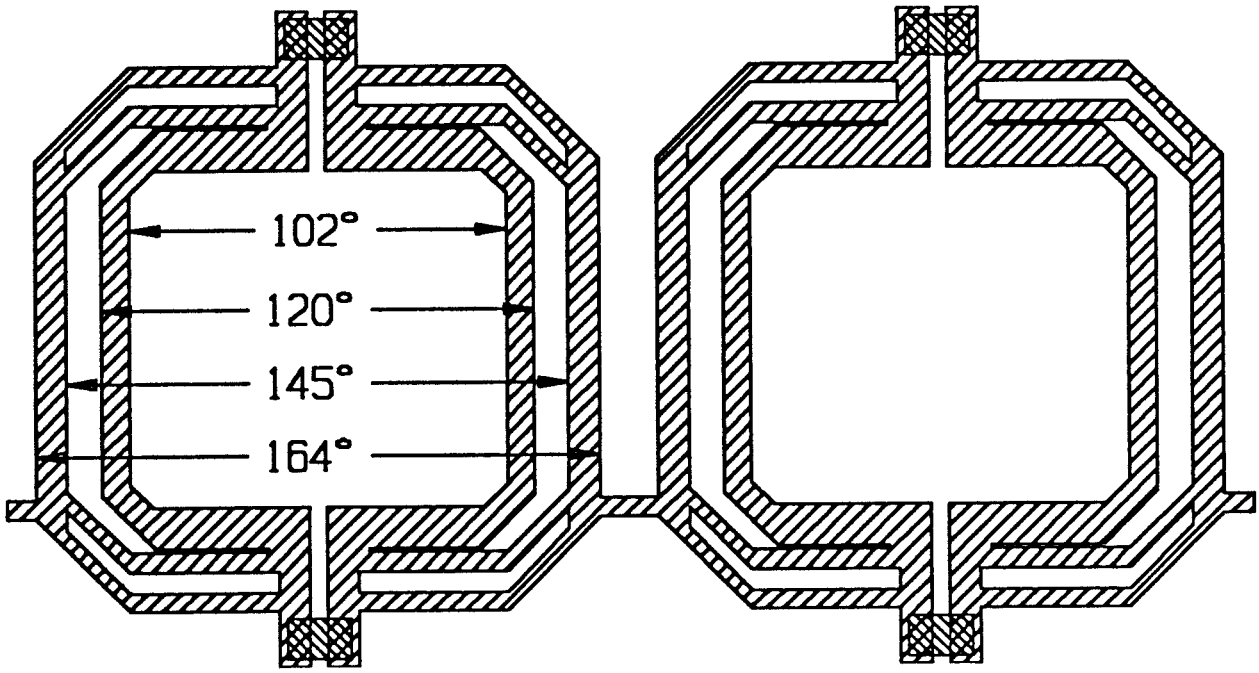

FIG. 1. Foil pattern for the split-half-turn (SHT) saddle coil—a simple modification of the Alderman–Grant resonator for improved transverse flux transparancy and B_1 homogeneity.

provides some transverse flux transparency with slightly improved σ, Q_L, and fd limit. It includes a crude attempt to improve current distribution by connecting several arcs in parallel to the outer bands, but over 60% of the current still follows the innermost path around the $\mathbf{B}_1$ axis, so B_1 homogeneity is not improved much, but transverse flux transparency is now sufficient to permit the satisfactory use of orthogonal coils. An approximate circuit model is shown in Fig. 2, in which the four tuning/segmenting capacitors ($C6$–$C9$) are approximately equal for minimum electric field near the center of the sample. These capacitors are shown in Fig. 1 displaced axially outward a small distance from the center of the arcuant foils to minimize their effects on B_0 homogeneity within the sample region, as this is generally important in microscopy. The subtended angles shown were determined by numeric modeling to give the best overall performance (σ, Q_L, η_F) for typical length and shield diameter ratios for orthogonal coils when sample losses dominate, but somewhat wider conductors perform better for small fd products. The coupled inductors ($L7$, $L8$) represent a balanced transmission line to the remote tuning, balancing, and matching elements, which often include inductors $L1$, $L2$ at very high frequencies.

Quadrature operation for circular polarization may be achieved by mounting two SHT coils orthogonally at slightly differing radii and driving with a quadrature hybrid, although it is more common for the orthogonal coil to be tuned to a different frequency for double resonance. With properly designed transmission lines to the tuning elements, the coils may be easily tuned over a frequency range of at least 15% by simply adjusting $C1$ (and another for an orthogonal coil) with little effect on σ, Q_L, or η_F. This is an order of magnitude greater tuning range than is possible using twice as many variables with the eight-rung BHP birdcage before its σ is severely degraded. Also, matching to widely different loads is much easier and less detrimental to σ than with the birdcage. We find this approach to double resonance to be considerably more effective in microscopy than the methods (*13, 14*) of double-tuning of birdcages we have evaluated. The measured and calculated values of η_F in experiment 2 (Table 1) show good agreement, and $\eta_F Q_L$ is comparable to that of typical, quadrature birdcages under similar conditions (*5*).

Of course, since most of the current still flows along the inner edge of the central flux window, B_1 homogeneity is significantly inferior to that of the precisely tuned 12-rung (or higher) single-resonance birdcage. Clearly, a more radical departure from conventional coil design is required for substantial improvements in tunability, σ, Q_L, η_F, and maximum fd product.

LITZ FOIL COILS

It is well known that a sinusoidal axial current distribution around an infinitely long cylinder produces a uniform transverse field, and multiturn saddle coils in NMR liquids probes for low frequencies position the wires or foil to approximate a sinusoidal current density. However, multiturn coils have too much inductance for fd products above several MHz-m. We noted in the previous section that the RF current will take the

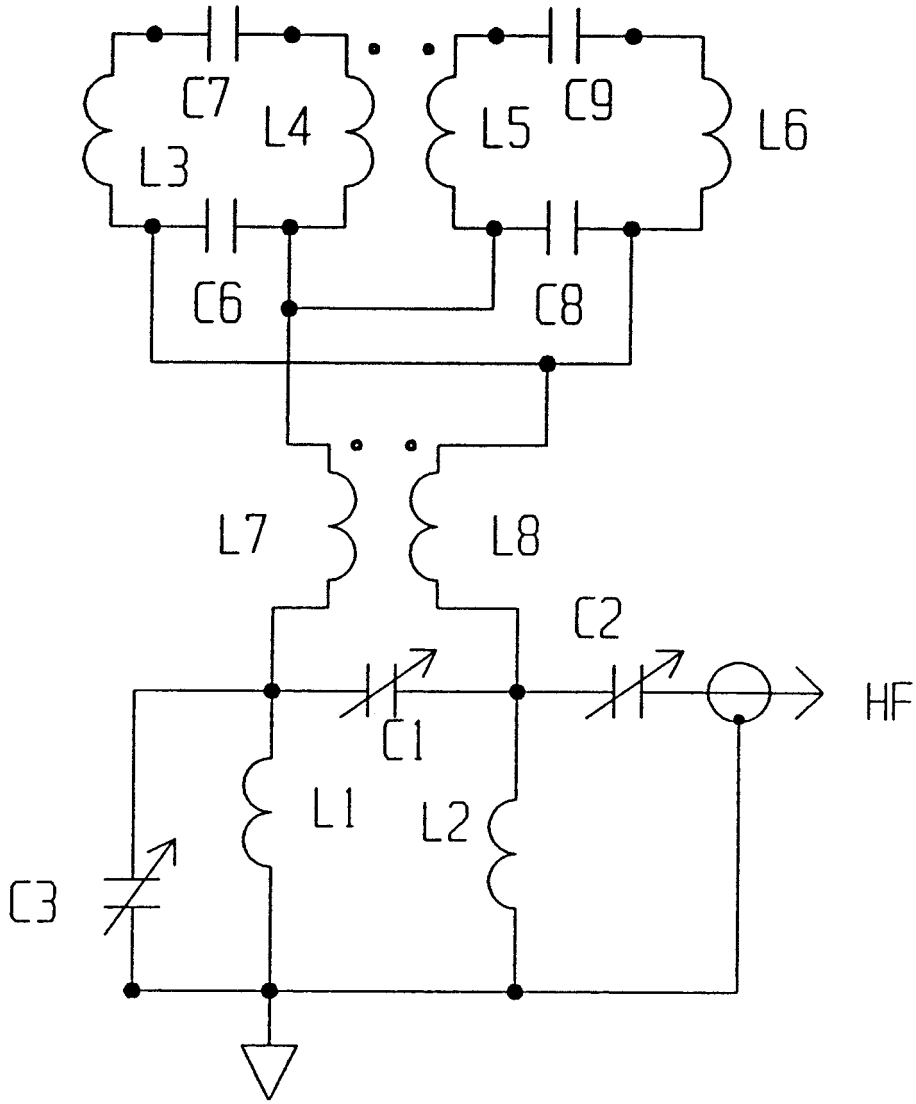

FIG. 2. A simplified RF circuit model of the SHT coil with remote tuning, balancing, and matching.

low-inductance (inside) route unless forced otherwise, so we desire an efficient way to reroute current in segmented single-turn resonators without using capacitive phase shifts. While the use of minimal coupling coefficients between adjacent loops in phased-array coils has advantages for localizing reception (*15*), high coupling coefficients offer the potential to control current densities as desired.

With relatively large coupling coefficients of parallel conductors it is possible to make extremely low inductance geometries behave magnetically more like multiturn coils in which the currents are redirected as desired—but without increasing inductive energy and thereby degrading filling factor. Expressed another way, electromagnetic software makes it possible to design coils in which the desired magnetic field profile is achieved by virtue of the coupling coefficients that arise solely from the coil geometry rather than from critical, capacitive phase shifters.

One way to understand the physical basis of the homogeneity limitation of the slotted resonator is to note that, since the divergence of **B** vanishes everywhere, in order for transverse B_1 to be uniform everywhere inside a cylinder, it must pass through the cylinder walls at every point along the perimeter. Hence, transparency of the coil to $\mathbf{B}_1$ is needed as well as transparency to flux perpendicular to $\mathbf{B}_1$ (for operation of orthogonal coils or for circular polarization). But RF flux cannot penetrate conductors—nor can it readily penetrate simple windows in conductors, as counter currents are induced according to Ampere's law.

Figure 3 illustrates two simple, two-element litz groups that provide the required flux transparency. The foils are joined at

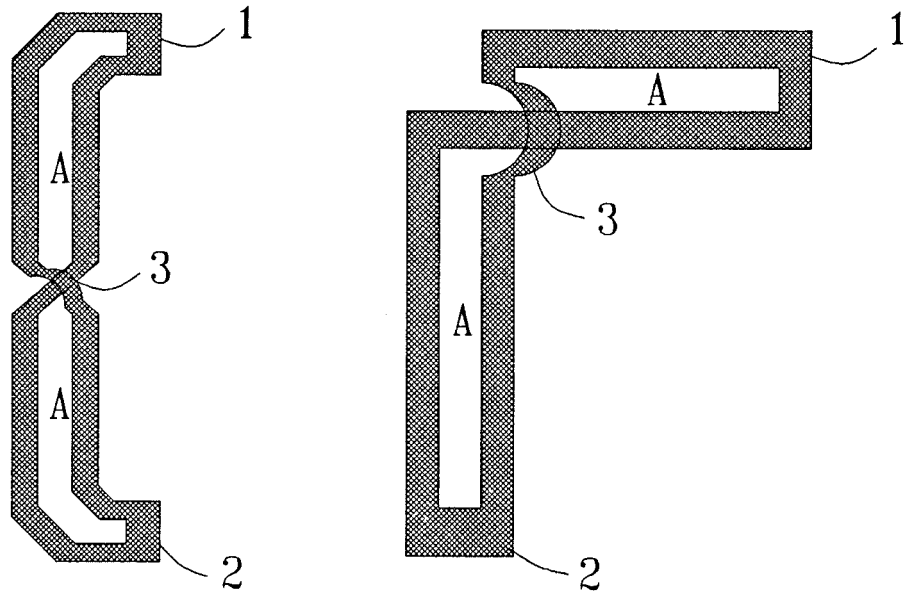

FIG. 3. Two basic two-element litz foil conductor groups for RF conduction between nodes 1 and 2 with flux transparency.

nodes at each end and have an electrically insulated crossover. If, for example, they are positioned in a uniform B_1 perpendicular to the plane of the paper, the areas A of the two flux-subwindows in each litz group must be equal (equal flux) for the groups to be transparent to the RF magnetic field—that is, to have no net current induced in the litz loops, although minor eddy currents will be induced within the foils. The litz group then functions as a transparent conductor from node 1 to node 2.

In actual practice, the litz groups will normally be in regions of nonuniform B_1 (by perhaps 5 to 30%) and minor adjustments in the areas may be beneficial so the differential current induced in the litz loops is small compared to the common mode current. However, the areas of the subwindows will usually be kept nearly equal.

Figure 4 illustrates the simplest step in the desired direction of reducing current crowding near the central flux-window: an insulated crossover is inserted between the inner and outer loops of the SHT coil near the center of each loop. Thus, half of the low-inductance inner route is placed in series with half of the high-inductance outer route. The two routes, by symmetry, must have equal inductance. Thus, they must have equal current. Their angular locations can now be readjusted at will, and the currents remain equal. For a homogeneous length 40% greater than the coil diameter, the optimum mean subtended angles of the inner and outer loops were numerically determined to be 96 and 156°, respectively, for moderate-width conductors, suitable for orthogonal coils. Not surprisingly, B_1 homogeneity is considerably improved compared to the SHT coil, and $\eta_F Q_L$ is also improved.

The next step is to carry the notion of insulated crossovers to its practical limits in generating the desired current distribution for optimum σ, Q_L, and η_F. Figure 5 illustrates a litz foil pattern with 20 insulated crossovers that evolved from a combination of numerical optimizations, symmetry arguments, and experiments. The coil is etched on double-clad laminate, such as copper-clad teflon. The top pattern is formed on the outside, the crossovers shown in the middle pattern are etched on the inside, and their superposition is depicted in the lower pattern, where the outside is shown in diagonal hatch and the inside is shown in a combination of square and slant hatch. The $\mathbf{B_0}$ axis and the sample cylinder axis are vertical. The pattern wraps completely around the cylinder, leaving two opposed, central, flux-windows on opposite sides. The $\mathbf{B_1}$ axis goes through the center of these central flux-windows. The photo in Fig. 6 shows it wrapped around a cylindrical coilform.

At first glance, it may appear that electric field couplings to the sample would be enormous, but we will soon show that capacitive segmentation to reduce the effects of stray capacitance and dielectric losses in the sample can usually address this problem more easily in litz coils than in the birdcage. Moreover, the segmentation need not significantly effect B_1 homogeneity as a function of frequency. However, we begin a detailed description with a moderate-frequency version. In this case, we place a number of parallel tuning capacitors across the two central tuning buses on each side and place shorts at all the other junctions between litz groups. We denote it the half-turn center-fed litz (CFL2) coil (we'll have a few comments on center-feeding later).

The coil's operation may be understood by following several current loops. Starting at the tuning capacitors at point A near the outside (that is, far from the a central flux-window), a current route goes up and over, through two high-inductance litz groups, then it crosses over (at CR) to the inside and goes

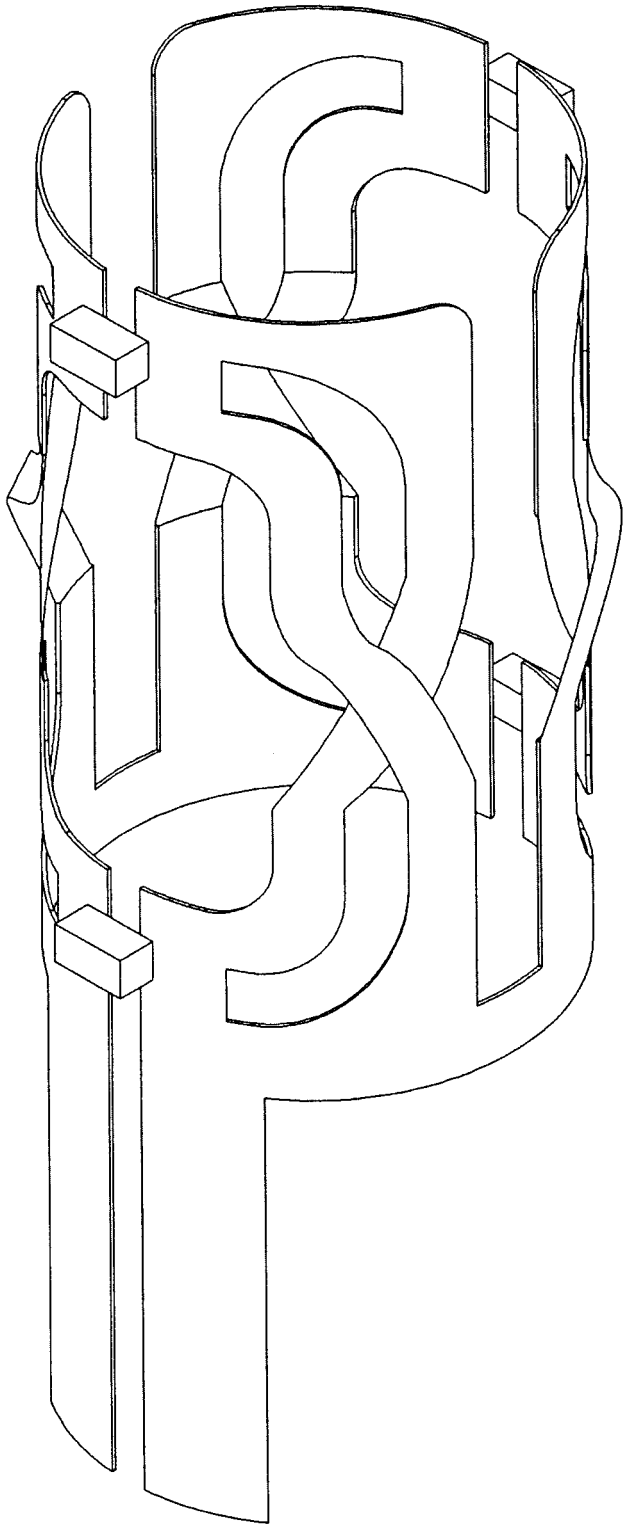

FIG. 4. Adding four insulated crossovers to the split-half-turn coil makes the simplest litz coil.

down through a low-inductance litz group to get to point *C* on the tuning capacitors on the opposite side. A parallel route starts up from point *B* through a low-inductance inner litz group, then crosses over (at CR) to the outside, and goes through two high-inductance litz groups to get to point *D* on the tuning capacitors on the opposite side. Obviously, these two routes have the same inductance, from symmetry, so the total currents in these two major routes must be equal. We have already noted that the currents in each path within each litz group are approximately equal. Hence, all subroutes carry approximately equal currents. The same applies to each quadrant.

Herein lies a major reason for the advantage of the litz coil: the high inductance of a portion of the outer loops is placed in series with the low inductance of a portion of the inner loops to limit current density along the inner edge of the central flux-window and achieve transparency of the windings. This means that only a relatively small fraction (typically 30%) of the total flux through the sample flows through the central flux-window, making it possible to redirect the current as needed and maintain uniform flux density throughout a much larger sample (*16*). Contrary to what might be initially expected from a serpentine pattern, both data and calculations show that both resistance and inductance are *reduced,* and Q_0, Q_L, and η_F are *increased.*

We have said nothing thus far about impedances because it was not necessary. The currents are approximately equal *independent* of frequency and tuning (in the long wavelength approximation). Thus, we can optimize the locations for best σ, Q_L, and η_F without concern about the effects of tuning on current distribution. (Of course, there is stray capacitance, which may be addressed through capacitive segmentation, as discussed later.) The coil we have just described we call the half-turn version because here, as in the Alderman–Grant and SHT coils described earlier, the current goes 180° around the B_1 axis between segmenting capacitors. For tuning to low frequencies, the segmenting capacitors on one side may be omitted (shorted), giving a one-turn CFL coil.

The optimum locations and widths of the azimuthal and axial conductor elements will vary depending primarily on the ratio of the sample length to its diameter and to a lesser extent on the ratio of the diameter of the external RF shield to the coil diameter d. Primary optimization criteria include maximizing η_F and Q_L while minimizing σ and RF fields beyond the ends of the homogeneous region.

While the optimum azimuthal subtended angle of the window in the KAG coil is ~90° (and ~100° for the SHT coil), the optimum azimuthal subtended angle of the central flux-window in the CFL coil is substantially less—typically ~55°. The optimum subtended angle of the outer edges of the outer axial conductor elements is nearly 180° when an orthogonal coil for quadrature detection or double resonance is not present. Optimum central window length is typically 85 to 90% of the sample length, compared to 105% for slotted resonators. Optimum spacing between the outer two axial elements is a little more than half of that between the inner two axial elements, as one would expect if trying to achieve a sinusoidal

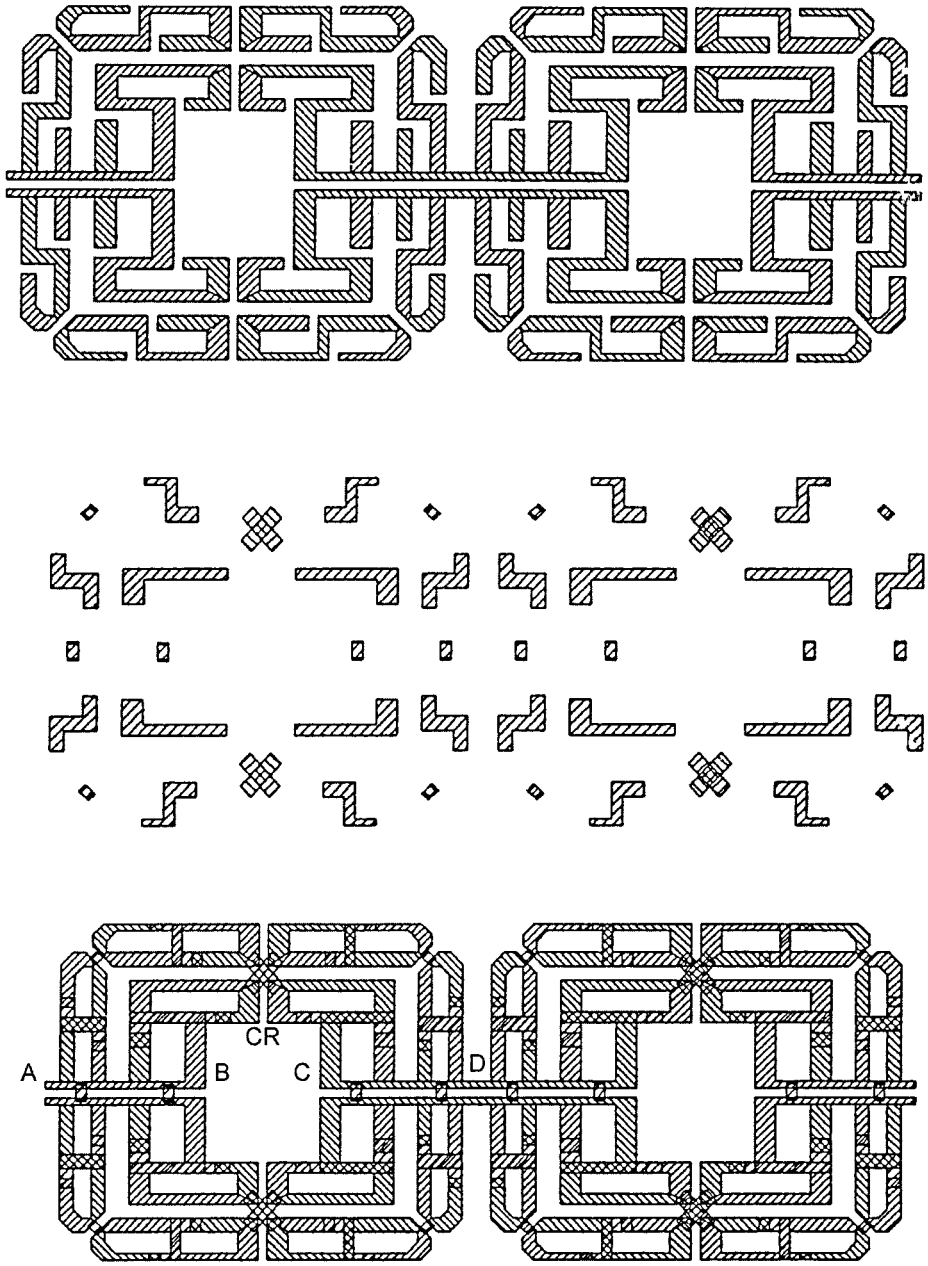

FIG. 5. The center-fed litz (CFL) pattern permits maximum tunability and homogeneity with 1, 2, 4, or 6 capacitors in each current path around the B_1 axis for *fd* products from 5 to 25 MHz-m.

distribution with constant-current elements. The requirement of comparable areas in the subwindows of each litz group then places rather tight constraints on the relative locations of the azimuthal members. When an orthogonal coil is present, the outer subtended angle may be reduced with acceptable loss in B_1 homogeneity, and ~170° is generally optimum. Also, additional changes in the symmetry are required, as the single crossover in the center at each end restricts orthogonal transparency between the main inner and outer loops.

At frequencies from dc to near self resonance, the optimized one-turn (unsegmented) litz coil with diameter d (in mm), external RF shield diameter sd, and central flux-window inside length h_1, has approximate total inductance L_T (in nH) as follows for typical conductor widths and length ratios:

$$L_T \cong 1.8(s - 0.95)(dh_1)^{0.5}/s. \quad [2]$$

Note that the constant coefficient has units of nH/mm, and s is dimensionless with a typical value of 1.15 to 1.5. The

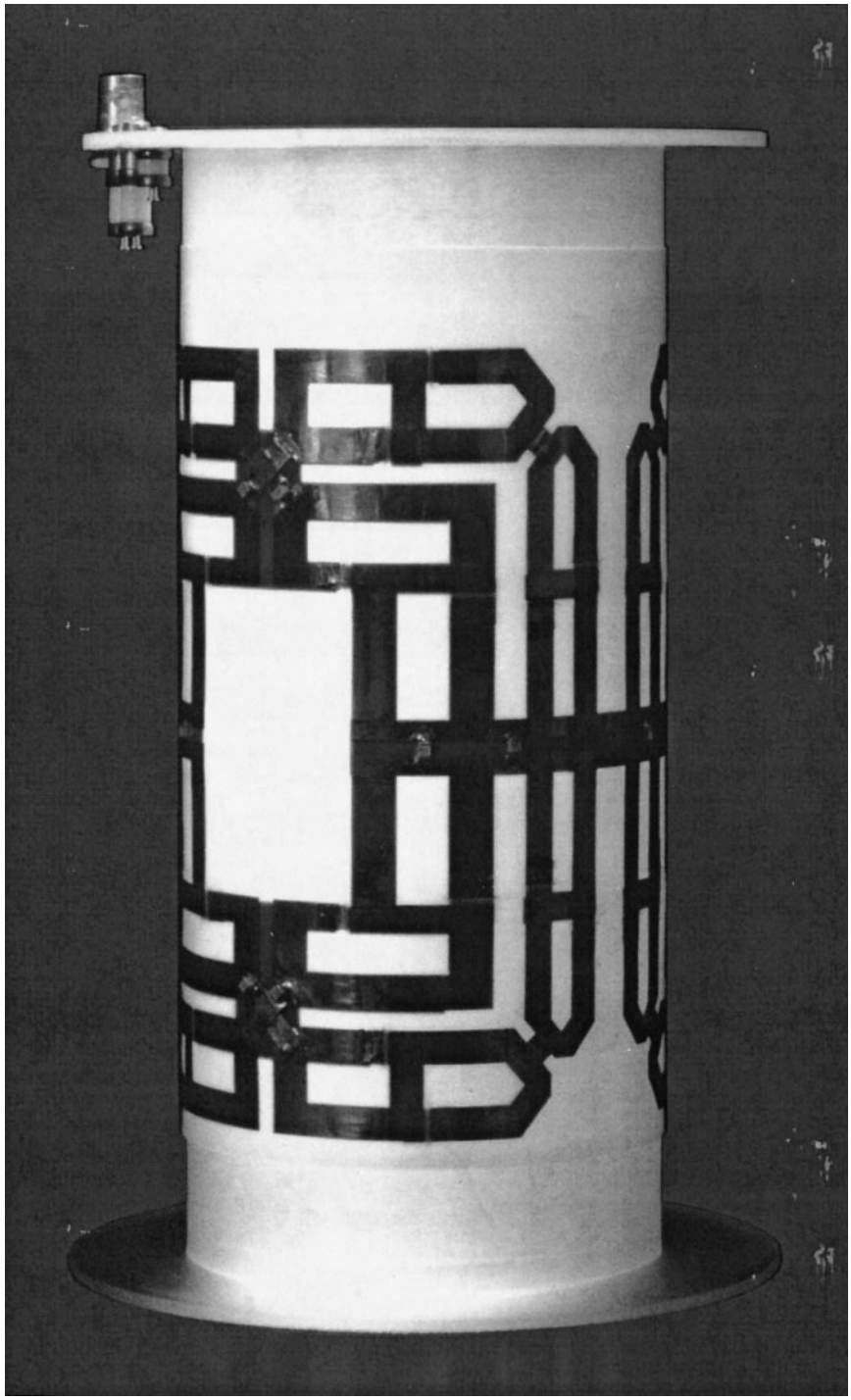

FIG. 6. Photo of litz coil of Fig. 5 wrapped around a cylindrical coilform.

inductance lies in the range from 3 to 200 nH for coils from 6 to 200 mm diameter with typical sample lengths and external RF shields. It is ~10% less than that of an unsegmented Kost coil for comparable applications. With a closely spaced external RF shield, self-resonance f_0 for the unsegmented version typically occurs for an $f_0 d$ product of 8–12 MHz-m, depending on various shielding details. As such, this coil has found applications in 10- to 70-mm MR $^{1}H/^{19}F$ microscopy coils and in multinuclear MRI/MRS microscopy coils ranging from 15 to 300 mm. In the larger sizes, the coil may be readily tuned over full multinuclear ranges using conventional methods with remote tuning capacitors without significant loss in sensitivity or

homogeneity if the leads are properly designed. In this case, the leads to the central tuning bus carry the full current, so their inductance must be minimized to maintain high η_F, and they must be shielded from the sample to prevent MRI signals near the gradient null point from folding back into the image.

MULTIPLE, CAPACITIVE SEGMENTATION

The discussion of the litz coil thus far has largely neglected frequency dependence, as the goal is to use symmetries that allow most electric field losses to be reduced through capacitive segmentation without affecting current distribution. The CFL2 coil of Fig. 5 (as described above) includes half-turn segmentation, similar to the KAG coil, except that the segmenting and tuning capacitors are located at the center (hence the name center-fed) rather than at the ends of the coil. Half-turn segmentation reduces stray capacitance (and associated sample dielectric losses) by a factor of 2 to 4 compared to the unsegmented CFL coil and extends its effective range upward by a factor of 1.5 to 1.9 (self-resonance product about 12–20 MHz-m). Placing the segmenting capacitors at the ends reduces electric fields in the sample, but the central location gives much better tunability by allowing a single capacitor adjustment to symmetrically tune both sides of the coil. Hence, it is better suited to highly variable loading and shielding, as encountered in flexible, wraparound applications, for example. Connecting the input RF lines at the center rather than at the ends also usually results in fewer problems with unwanted modes, especially when an orthogonal multinuclear coil is present (*17*). The CFL2 coil has found applications for $^1H/^{19}F$ as well as fully multinuclear applications. A 100-mm CFL2 coil, for example, tuned easily over the full range of 50–150 MHz with no significant loss in S/N or σ and no difficulty in matching to the full range of loads.

It is beneficial to shield the sample from the electric field, which is greatest near the tuning capacitors. If the coil is electrically balanced, effective shielding may be accomplished with guard rings or shield strips, which have the added beneficial effect of reducing the effects of cross-currents. The interloop stray capacitors in the cross-current shield patches may contribute to additional modes, but they need not interfere with tuning, as they are usually further from the homogeneous mode than are, for example, parasitic modes in a birdcage.

The symmetry of the litz coil allows the capacitive segmentation to be easily taken several steps further. Segmenting capacitors may be inserted between two litz groups at the corners, for example, in each octant for a quarter-turn version (CFL4). Effects of stray capacitance and dielectric losses are reduced again, and the frequency range is extended upward by another factor of about 1.2 to 1.5, making its self-resonance *fd* product in the range of 15 to 30 MHz-m. This coil has worked well for ^1H–^{19}F mice microscopy at 300 to 500 MHz and rats at 200 to 300 MHz.

Because the corner segmenting capacitors in the CFL4 coil control current balance between parallel members that are nearly resonant, they must be matched (within each pair) to within ~1% or B_1 homogeneity will be somewhat degraded. This is comparable to the requirement for all of the capacitors in a birdcage, and it implies that it is not practical to make these segmenting capacitors user-variable. Hence, the tuning range of the CFL4 coil is typically limited to about 10% by adjustments of just the central tuning capacitors. (More symmetric coils patterns are now being used that do not require precision matching for quarter-turn segmentation and have considerably better transverse transparency for improved H/X operation.) Additional segmenting capacitors may be inserted at the junctions between the litz groups at the crossovers (CR) for a sixth-turn version (CFL6) for higher frequency operation.

Experiment 3 in Table 1 shows some data for a CFL2 coil for sample length and diameter 80% of the coil diameter with $s = 1.4$. For this coil, σ is actually a little better than that of the perfectly tuned 16-rung linear birdcage and it is considerably better than that of the typical birdcage (*5*). A large part of the reason is that the effects of tuning errors and input couplings are much less, but also, the current densities in the end arcs are controlled and distributed in a more optimal manner. Again, even though filling factor for linear polarization is divided by 2 compared to circular, relative SNR—$(\eta_F Q_L)^{1/2}$—of this coil is about 30% better than that of an optimized quadrature birdcage we compared it to, and it compares even more favorably at lower *fd* products. The primary reason appears to be that maximum axial RF magnetic field in the sample near the end edges is only one-third as large as in birdcages. Hence, inductive loss in sample material in this region is reduced. Capacitor and coil losses are also lower in the litz coils, which is important for light loads. (Note that Q_{LS} is 291 with a 70-mm spherical saline sample.)

Experiments 4 through 6 show performance of a moderately short 100-mm litz coil at frequencies from 70 to 134 MHz, and experiments 7 through 9 show litz coil results under various conditions at 200 MHz to facilitate direct comparisons with previously tested birdcages under similar conditions (*5*). For comparisons at different frequencies when Q_L is explicitly included, the more complete relative SNR is $f_0^{3/2}(\eta_F Q_L)^{1/2}$ (*18*).

THE CFL6 COIL RF CIRCUIT MODEL

The simplified RF circuit model shown in Fig. 7 may look foreboding at first, but it should help bring into focus the major reasons for the insensitivity of these coils to sample loading and other tuning errors. The coils are designed to achieve the desired current distribution via symmetries and mutual inductances that depend only on geometry and permeability in a way that easily permits symmetric capacitive segmentation. Since the permeability of any MR sample is 1.0000, we are left only with perturbations from shield asymmetries, other coils, and stray capacitance effects. The conductor paralleling and high-

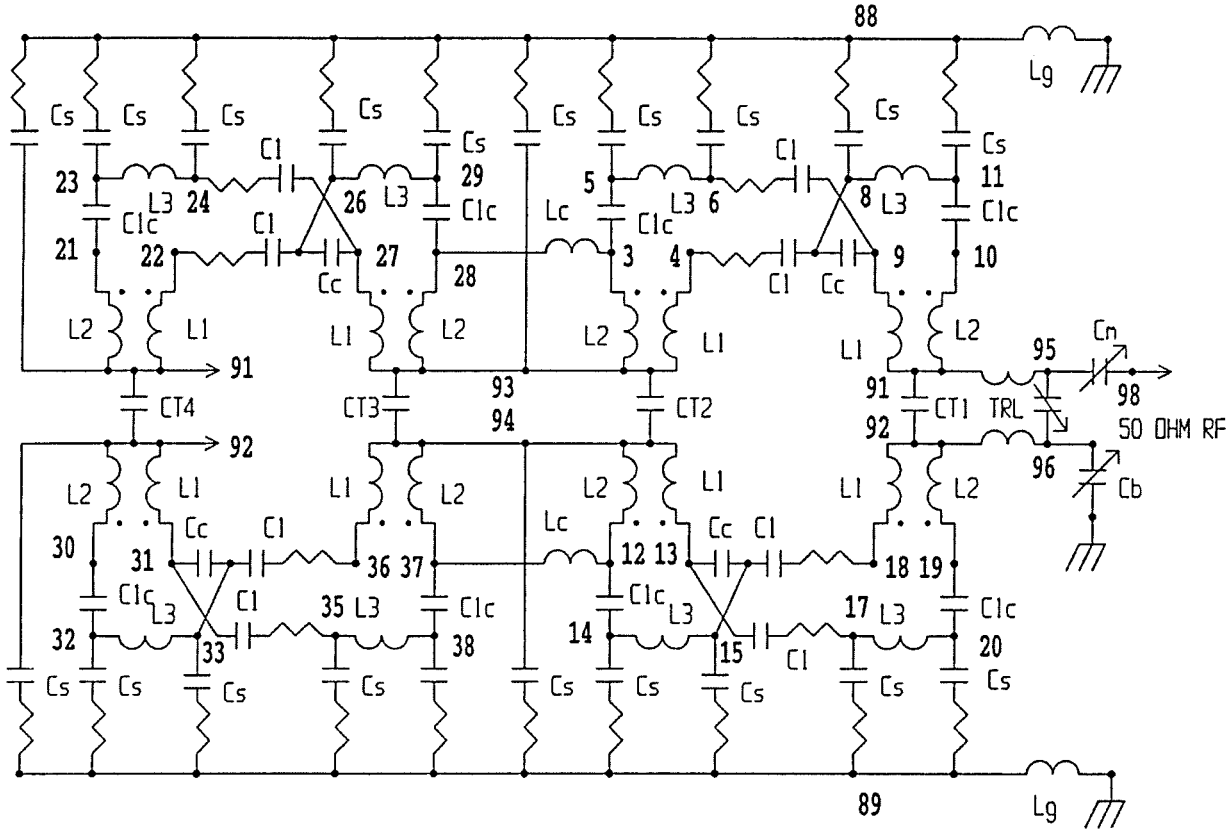

FIG. 7. An approximate RF model for the CFL6 coil showing major parasitics.

order segmentation makes impedances at the central tuning nodes (the C_T's) in the CFL6 much lower than even in the balanced-band-pass birdcage, so dielectric detuning effects are reduced (for a given $\eta_F Q_L$). A large adjustment in any C_T has negligible effect on either the electric field balance or the current distributions. (Each C_T would normally consist of at least two parallel fixed capacitors for reduced parasitics.) Each litz group is represented as a single inductor (L_1, L_2, L_3), and input coupling is also shown. Normal tuning and matching is achieved with just two capacitor adjustments, though for major shifts it may be necessary to adjust two C_T's, C_B, and C_M.

In the absence of external coupling, the inhomogeneous modes, the lowest of which may be below the homogeneous mode if $C_S > C_1$, are easy to keep away from the homogenous mode as long as the coil is well balanced—even if crossover capacitance C_C is comparable to (or even slightly larger than) C_1. Normally, $C_{T2} = C_{T3} = C_{T4} \cong 2C_1$, and C_{T2} is two to three times (depending on C_S/C_1) the capacitance needed to resonate the effective total inductance L_T as estimated by Eq. [2]. For the conditions of experiment 6, for example, $L_1 \cong L3 \cong 0.7L_2 \cong 0.44L_T$ and the L_2:L_1 coupling coefficient is ~0.36, but these values vary considerably, depending on length-to-diameter ratios and shield-to-diameter ratios. For capacitive matching as shown, $C_{T1} \cong CT3 - C_M/2$ and $C_M \sim C_B$, but C_B is not critical, as the total C_S is normally much larger. The schematic is only an approximation, as most of the inductors are strongly coupled to two other inductors and weakly coupled to all other inductors. Since our circuit software (*19*) does not handle mutual inductance between more than two inductors at a time, we included paralleling tabs L_C to account for the strong coupling between the semicoils. Not having fully adequate RF software or accurate knowledge of the various elements is not a serious handicap (at least in the long wavelength approximation), as B_1 homogeneity is assured from symmetry as long as the various C_1's are equal. Their relationship to the C_T's primarily affects sample dielectric loss, which is minimized when each inductor is approximately balanced with respect to ground. This occurs when the voltages across each capacitor are roughly equal. When stray capacitances are negligible, this condition is achieved when $C_1 = C_{1C} = C_T/2$.

Directly coupled matching is normally avoided in the birdcage because it exacerbates ground-loop problems and increases losses if the coil is not very well balanced (*5*). However, such matching is an integral part of the litz coil design, as it is the best way to obtain the order-of-magnitude increase in tuning range. The transmission line TRL shown in Fig. 7 (and any additional parasitic capacitance and inductance) leading to the remote tuning, balancing, and matching variable capacitors must be well characterized for the RF circuit model to be useful

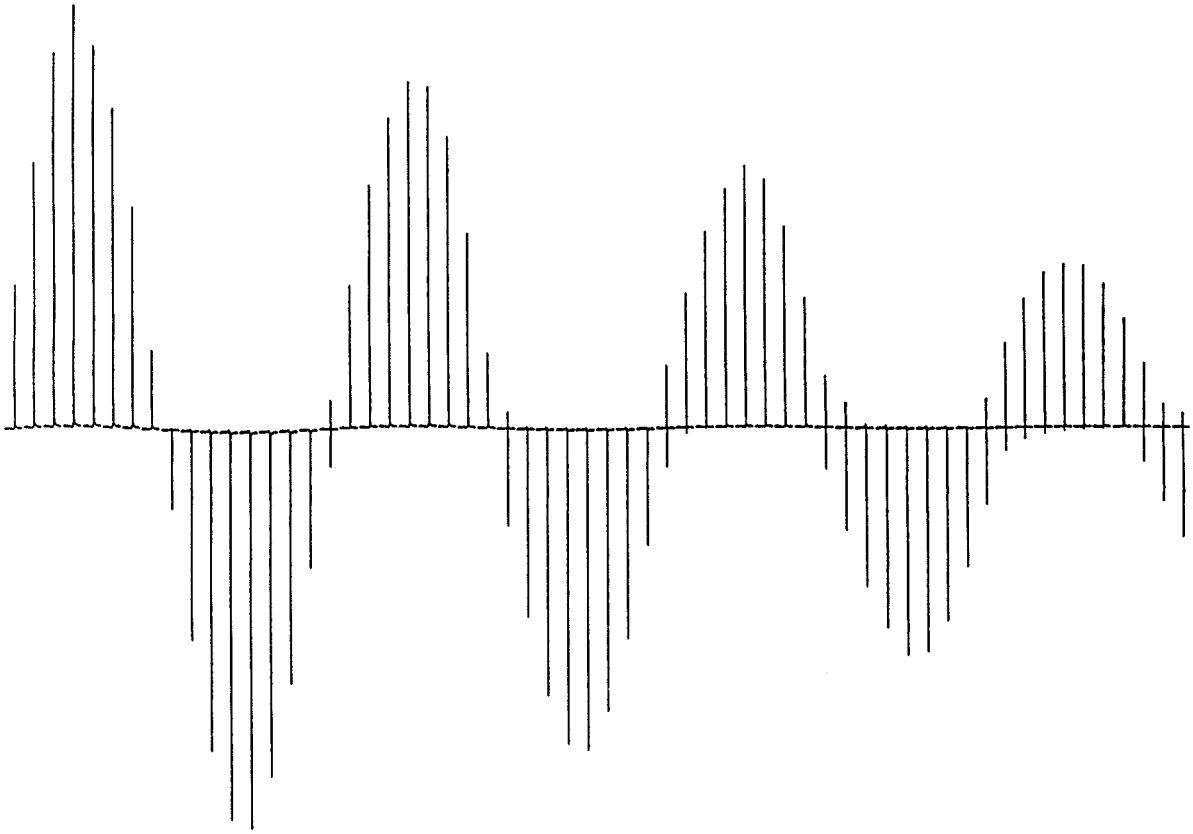

FIG. 8. Pulse width array from a half-turn litz coil with water sample of diameter 0.88 *d* and shield diameter 1.22 *d*.

in predicting parasitic modes and tuning range. In most cases, special effort is required to make the transmission line with sufficiently high propagation factor, low attenuation constant, and optimum impedance.

As with the birdcage, if the coil is not balanced, coupling to ground (C_G) can be quite troublesome. The input TRL must be positioned such that the common mode induced by nearby coil conductors is minimized. Then, balance in the litz coil may be easily adjusted without concern about the effect of that adjustment on B_1 homogeneity. The circuit model and our experience suggest the local effect on homogeneity of perturbing a C_S at either end is an order of magnitude less than in the BHP birdcage *and* the effect is much more localized to the octant of the perturbation. Perturbations near the center of the CFL6 litz coil (or anywhere in the CFL2 coil) are even less significant—unless an inhomogeneous mode is nearby. The deficiencies of the RF model (not properly including all of the mutual inductances) become significant at high *fd* products, especially with relatively long transmission lines ($>\lambda/6$) to the tuning network. We find, for example, that the ratio of current through L_1 to that through L_2 increases at high *fd* in the CFL4 coil more rapidly than predicted by the model and this requires minor adjustments in the conductor locations to maintain optimum σ.

Finally, we note that a litz conductor group by definition does not include a capacitor of significant RF reactance—it is a broad-banded transparent conductor from one node to another and the RF capacitors are always inserted between litz groups. The litz group is transparent only to a specific (substantially uniform) field profile—not the gradient field. Thus, gradient eddy current problems may arise unless proper measures are taken (*8*). In most cases, the conductors may be made of foil thin enough to avoid these problems without significantly affecting Q_L. When this is inadequate, audio blocking capacitors may be inserted into the litz groups to suppress gradient eddies with little effect on RF performance.

NMR/MRI TEST RESULTS

The array of NMR spectra of variable pulse widths in Fig. 8 from our first litz coil with sample diameter 88% of the coil diameter demonstrates the high B_1 homogeneity of the litz coil. The single-pulse, proton Bloch decay NMR spectra are arrayed sequentially as the RF pulse width is increased in 9-μs increments from 9 μs to over 500 μs with 5-s recycle delays between spectra. The spectra were acquired at 7.06 T on a saline sample 36 mm in diameter, 25 mm in length, inside a 41-mm-diameter litz coil with $h_1 = 27$ mm and a 50-mm external RF shield diameter. Note that the amplitude of the 4.5π (810°) pulse is over 60% of the amplitude of the $\pi/2$ pulse, which essentially corroborates the calculated σ. Over the

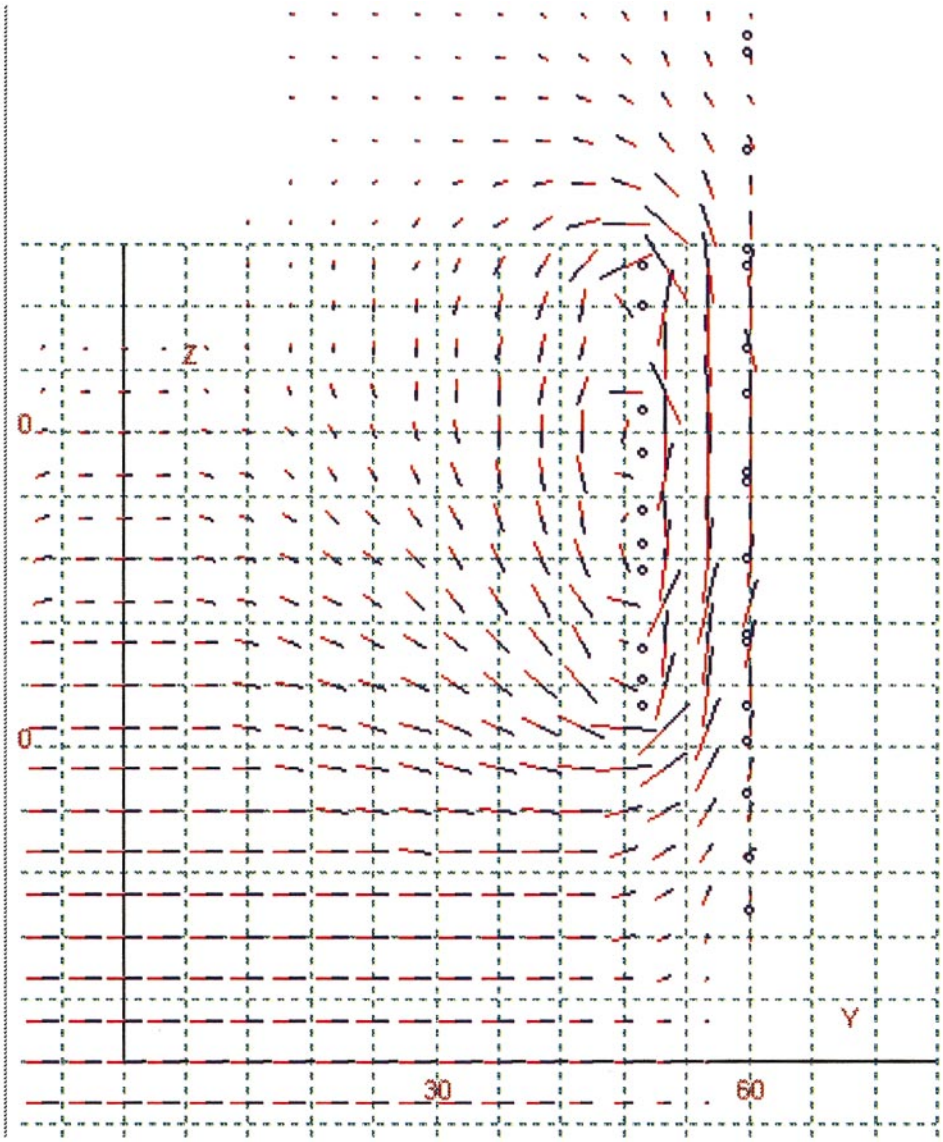

FIG. 9. Transverse view of the B_1 field projections for the litz coil.

past 3 years, this RF coil and gradient set has been used in a number of systems at fields from 200 to 500 MHz for mice microscopy in 89-mm vertical bore magnets with 73-mm RT shims. Both sensitivity and homogeneity are reported to be better with the 40-mm 400 MHz ^{1}H–^{19}F linear litz coil than with fixed-tuned eight-rung quadrature birdcages under similar conditions (*20*).

Similar results have been obtained for a wide variety of sizes with sample diameters generally over 82% of the coil diameter and shield diameters usually less than 1.4 times the coil diameter at frequencies from 10 to 600 MHz (*21*). In the single-resonance cases, the coils were etched according to numerical optimizations without experimental fine tuning for B_1 homogeneity. Spectral resolution better than 0.05 ppm has also been achieved, even with large samples, by including relatively simple magnetic compensation methods for the central chip capacitors (*7*).

Figure 9 illustrates the magnetic field vector projections, as calculated by our augmented Biot-Savart software, for a 100-mm litz coil in the *YZ* plane for $x = 0$, and Fig. 10 depicts the magnetic field vector projections in the *XY* plane for $z = 0$. The litz coil conductor sections are represented by the closely spaced small circles at a radius of 50 mm. The external shield has a radius of 60 mm, where induced current elements are also represented by small circles. Note that the flux through the central flux-window is a minor fraction of the total. Figure 11 shows a color scale representation of the transverse magnitude of a CFL6 coil with $s = 1.2$.

Figure 12 shows a cross-section without intensity correction of a postmortem human cervical spinal cord (14-mm sample

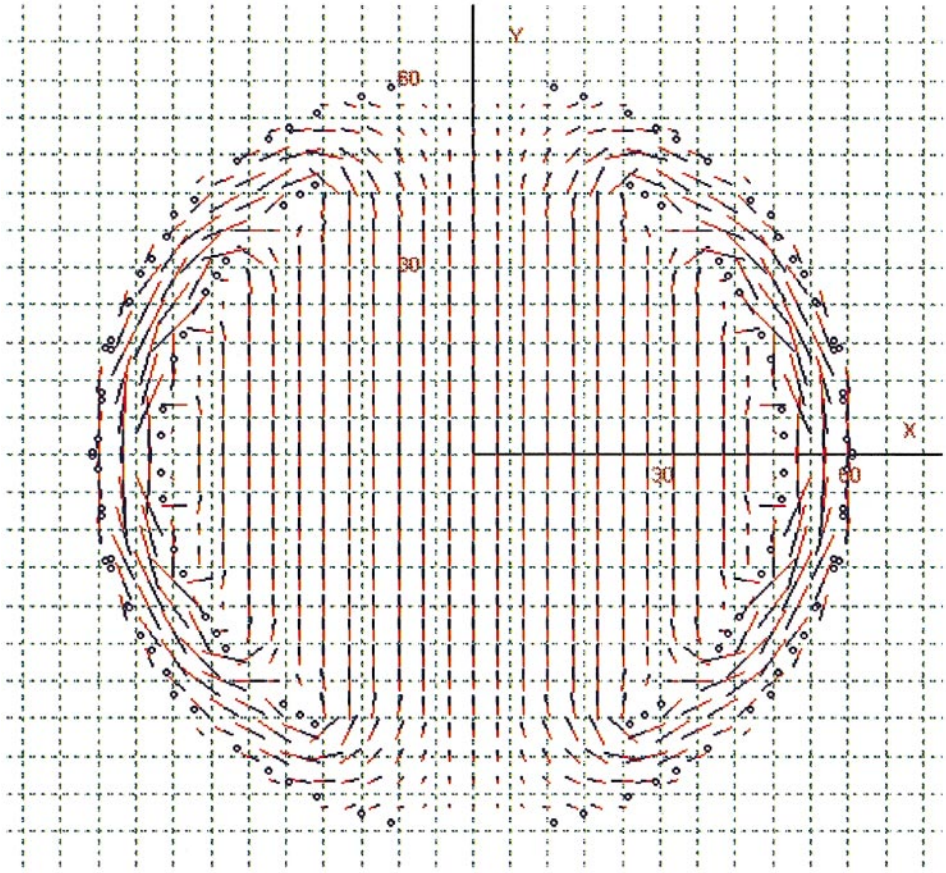

FIG. 10. Axial view of the B_1 field projections for the litz coil.

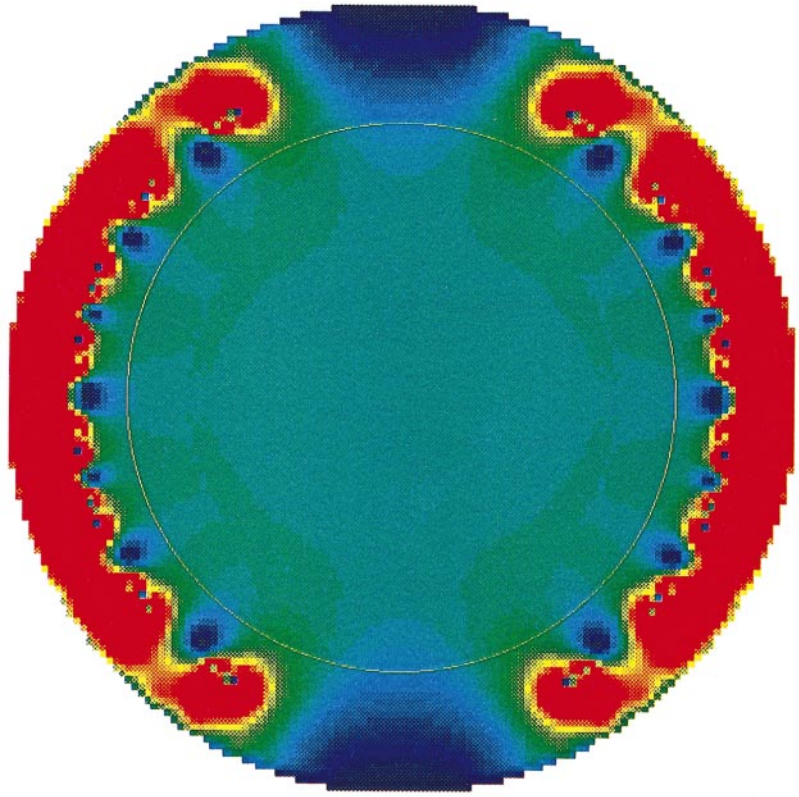

FIG. 11. Transverse B_1 magnitude of a CFL6 coil with $s = 1.2$ depicted using a color scale.

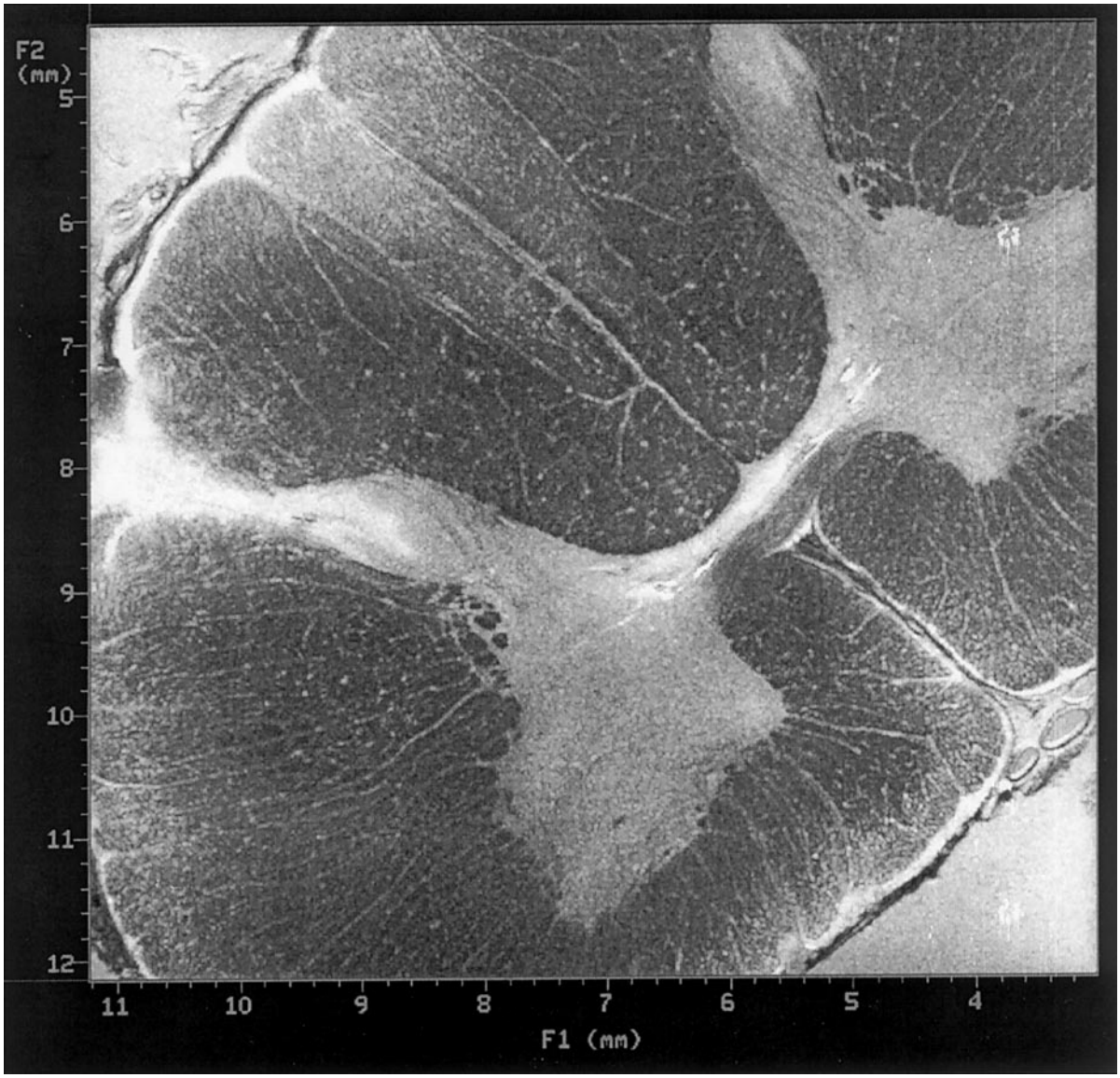

FIG. 12. Human cervical spinal cord ^{1}H image with 20-μm resolution taken with a 16-mm litz coil in a ^{1}H/X probe at 600 MHz in a narrow-bore magnet.

diameter) taken with a 16-mm ^{1}H litz coil inside an orthogonal 19-mm multinuclear litz coil. Both coils were inside the 24-mm RF shield in a gradient set (Doty Scientific, model 24-40) for use inside the RT shims (with 40-mm bore) in a 600-MHz spectroscopy magnet (52-mm RT bore). In-plane resolution of ~20 μm was obtained on a 0.1-mm slice in about 10 h (*21*). The multinuclear coil was tunable from ^{31}P to ^{2}H with B_1 homogeneity somewhat better than that of the ^{1}H coil. Contrast-to-noise, B_1 homogeneity, resolution, and SNR appear to compare favorably to recently reported results using a single-resonance superconducting RF coil on a sample volume smaller by a factor of ~10 (*22*), even though SNR generally scales inversely with total sample volume for a constant voxel size when sample losses dominate.

CONCLUDING REMARKS

Numerical and experimental data for several slotted resonators and linear litz coils were presented. In all cases for *fd* up to 20 MHz-m, *d* up to 100 mm, with external shield diameters up to 1.4 *d*, the data suggest that the linear litz coil should have better sensitivity and homogeneity (often by ~30%) than the quadrature birdcage. Moreover, the linear litz coils have an order-of-magnitude-larger tuning range, and capacitor value variations of 10 to 20% are generally inconsequential except in certain positions in the more highly segmented coils. The only apparent disadvantage of the litz coil is that its optimum overall length is a little greater than the birdcage's for a given sample length and this sometimes impedes sample access, but the

coil's end regions may be compressed axially with little loss in SNR or homogeneity when necessary.

In double-resonance applications, we have thus far evaluated only linear double-resonance multinuclear orthogonal litz coils (*21*) and double-tuning of litz coils by conventional methods. The advantages of the litz coil appear to be substantial for these applications and for cases with highly variable loads.

Very recent experiments with new litz coil patterns appear promising for quadrature coils with *fd* product at least up to 35 MHz-m and will be reported in due course. Preliminary results also suggest that related coil design methods may be effective in addressing the central brightening that characterizes conventional birdcages as the wavelength within the sample approaches its diameter (*23*). Work is beginning in this area, where long-wavelength assumptions break down.

ACKNOWLEDGMENTS

The authors thank the Center for Structural Biology at the University of Florida for the spinal cord image and Y. Kanazawa for the motivation to advance MRI coil technology. The authors also thank numerous technicians and engineers at (or formerly at) Doty Scientific, especially Xunming Chen, Andy Yang, David McCree, John Staab, Jiong Shao, Art Boman, Vince Cothran, and Mark Moore for their assistance in programming, experiments, calculations, analysis, and prototyping. This work was supported by Doty Scientific, Inc.

REFERENCES

1. J. Tropp, The theory of the bird-cage resonator, *J. Magn. Reson.* **82,** 51–62 (1989).
2. J. Tropp, The theory of an arbitrarily perturbed bird-cage resonator, and a simple method for restoring it to full symmetry, *J. Magn. Reson.* **95,** 235–243 (1991).
3. J. T. Vaughan, H. P. Hetherington, J. O. Otu, J. W. Pan, and G. M. Pohost, High frequency volume coils for clinical NMR imaging and spectroscopy, *Magn. Reson. Med.* **32,** 206–218 (1994).
4. J. S. Tropp, Method of correcting an asymmetry in an NMR radio frequency coil and an improved radio frequency coil having N-fold symmetry and reduced eddy current, U.S. Patent No. 5,196,797 (1993).
5. F. D. Doty, G. Entzminger, C. Hauck, and J. P. Staab, Practical aspects of birdcage coils, *J. Magn. Resn.* **138,** 144–154 (1999).
6. O. Ocali and E. Atalar, Ultimate intrinsic signal-to-noise ratio in MRI, *Magn. Reson. Med.* **39,** 462–473 (1998).
7. F. D. Doty, G. Entzminger, and Y. A. Yang, Magnetism in HR NMR probe design. I: General methods, *Concepts Magn. Reson.* **10,** 133–156 (1998).
8. F. D. Doty, *in* "Optimization of MRI Gradient Coils in Spatially Resolved Magnetic Resonance," (P. Blumler, B. Blumich, R. E. Botto, and E. Fukushima, Eds.), Wiley–VCH, Weinheim (1998).
9. J. M. Jin and J. Chen, On the SAR and field inhomogeneity of birdcage coils loaded with the human head, *Magn. Reson. Med.* **38,** 953–963 (1997).
10. L. F. Fuks and W. A. Anderson, Perturbation method for finding the RF field on an NMR probe, Poster presented at ENC in Orlando, FL (1997).
11. D. W. Alderman and D. M. Grant, An efficient decoupler coil design which reduces heating in conductive samples in superconducting spectrometers, *J. Magn. Reson.* **36,** 447–451 (1979).
12. G. J. Kost, S. E. Anderson, G. B. Matson, and C. B. Conboy, A cylindrical-window NMR probe with extended tuning range for studies of the developing heart, *J. Magn. Reson.* **82,** 238–252 (1989).
13. J. R. Fitzsimmons, B. L. Beck, H. R. Brooker, Double resonant quadrature birdcage, *Magn. Reson. Med.* **30,** 107–114 (1993).
14. A. Amari, A. M. Ulug, J. Bornemann, P. C. M. van Zijl, and P. B. Barker, Multiple tuning of birdcage resonators, *Magn. Reson. Med.* **37,** 243–251 (1997).
15. P. B. Roemer, W. A. Edelstein, C. E. Hayes, S. P. Souza, and O. M. Mueller, The phased array, *Magn. Reson. Med.* 16, 192–225 (1990).
16. F. D. Doty, Low inductance transverse litz foil coils, Patents pending, PCT No. WO 97/26560 (1997).
17. F. D. Doty and G. Entzminger Jr., Center-fed paralleled saddle coils for multinuclear double-resonance NMR or MRI, Patent pending, PCT No. WO 97/33185 (1997).
18. F. D. Doty, Probe design and construction, *in* "Encyclopedia of NMR," Vol. 6, Wiley, New York (1996).
19. ARRL Radio Designer 1.5, formerly Compact Software Inc., Patterson NJ, recently acquired by Ansoft, Pittsburgh, PA.
20. Yoko Kanazawa, Pharmaceutical Sciences, Kyusha Univ., Fukuoka, Japan, private communication.
21. S. J. Blackband, J. D. Bui, D. L. Buckley, T. Zelles, H. D. Plant, B. A. Inglis, and M. I. Phillips, MR microscopy of perfused brain slices, *Magn. Reson. Med.* **38,** 1012–1015; B. Inglis, L. Yang, D. Plant, E. Wirth, and T. Mareci, Diffusion tensor micro-imaging of excised human spinal cord. ISMRM-97, Poster No. 505, Vancouver.
22. S. E. Hurlston, W. W. Brey, S. A. Suddarth, and G. A. Johnson, A high-temperature superconducting helmholtz probe for microscopy at 9.4 T, *Magn. Reson. Med.* **41,** 1032–1038 (1999).
23. D. C. Alsop, T. J. Connick, G. Mizei, A spiral volume coil for improved RF field homogeneity at high static magnetic field strength, *Magn. Reson. Med.* **40,** 49–54 (1998).